PNAS RESEARCH ARTICLE | MICROBIOLOGY OPEN ACCESS

Cryo-EM structures of wild-type and E138K/M184I mutant HIV-1 RT/DNA complexed with inhibitors doravirine and rilpivirine

Abhimanyu K. Singh[a,b], Brent De Wijngaert[a,b], Marc Bijnens[a,b], Kris Uyttersprot[a,b], Hoai Nguyen[c,d], Sergio E. Martinez[a,b], Dominique Schols[a,b], Piet Herdewijn[c,d], Christophe Pannecouque[a,b], Eddy Arnold[e,f], and Kalyan Das[a,b,1]

Edited by William Jorgensen, Yale University, New Haven, CT; received March 1, 2022; accepted June 1, 2022

Structures trapping a variety of functional and conformational states of HIV-1 reverse transcriptase (RT) have been determined by X-ray crystallography. These structures have played important roles in explaining the mechanisms of catalysis, inhibition, and drug resistance and in driving drug design. However, structures of several desired complexes of RT could not be obtained even after many crystallization or crystal soaking experiments. The ternary complexes of doravirine and rilpivirine with RT/DNA are such examples. Structural study of HIV-1 RT by single-particle cryo-electron microscopy (cryo-EM) has been challenging due to the enzyme's relatively smaller size and higher flexibility. We optimized a protocol for rapid structure determination of RT complexes by cryo-EM and determined six structures of wild-type and E138K/M184I mutant RT/DNA in complexes with the nonnucleoside inhibitors rilpivirine, doravirine, and nevirapine. RT/DNA/rilpivirine and RT/DNA/doravirine complexes have structural differences between them and differ from the typical conformation of nonnucleoside RT inhibitor (NNRTI)–bound RT/double-stranded DNA (dsDNA), RT/RNA–DNA, and RT/dsRNA complexes; the primer grip in RT/DNA/doravirine and the YMDD motif in RT/DNA/rilpivirine have large shifts. The DNA primer 3′-end in the doravirine-bound structure is positioned at the active site, but the complex is in a nonproductive state. In the mutant RT/DNA/rilpivirine structure, I184 is stacked with the DNA such that their relative positioning can influence rilpivirine in the pocket. Simultaneously, E138K mutation opens the NNRTI-binding pocket entrance, potentially contributing to a faster rate of rilpivirine dissociation by E138K/M184I mutant RT, as reported by an earlier kinetic study. These structural differences have implications for understanding molecular mechanisms of drug resistance and for drug design.

polymerase | NNRTI | drug resistance | drug design | electron microscopy

Significance

The enzyme reverse transcriptase (RT) is a key antiviral target, and nonnucleoside RT inhibitors (NNRTIs) are among the frequently used components of antiretroviral therapy for treating HIV-1 infection. The emergence of drug-resistant mutations continues to pose a challenge in HIV treatment. The RT mutations M184I and E138K emerge in patients receiving rilpivirine. We obtained the structural snapshots of rilpivirine, doravirine, and nevirapine inhibited wild-type and M184I/E138K RT/DNA polymerase complexes by cryo-electron microscopy. Key structural changes observed in the rilpivirine- and doravirine-bound structures have implications for understanding NNRTI drug resistance. Additionally, the cryo-EM structure determination strategy outlined in this study can be adapted to aid drug design targeting smaller and flexible proteins.

The emergence of drug resistance continues to be a challenge in long-term management of HIV-1 infection. Extensive research on HIV over four decades has helped in improving the treatment options and quality of life for HIV-infected individuals. More than 30 drugs have been approved, and various drug combinations are used to treat the infected individuals under antiretroviral therapy regimens (1, 2); currently, over 27 million individuals are taking antiviral drugs (WHO, 2021; https://www.who.int/news-room/fact-sheets/detail/hiv-drug-resistance). The individual drugs target specific functional steps in the lifecycle of the virus, such as viral attachment and fusion, reverse transcription, integration of viral DNA to the host-cell DNA, and maturation of newly formed immature virions (3, 4). A major challenge in prolonged antiviral treatment is the emergence of drug-resistant mutant strains. The mutations that confer resistance to a drug commonly appear in the targeted protein, and often the mutations directly or indirectly affect the binding of a drug.

The viral enzyme reverse transcriptase (RT) copies the viral single-stranded RNA to a double-stranded DNA (dsDNA). RT is targeted by 14 Food and Drug Administration–approved drugs, of which 8 are nucleoside RT inhibitors (NRTIs) (5) and 6 are nonnucleoside RT inhibitors (NNRTIs)—nevirapine (NVP), delavirdine, efavirenz (EFV), etravirine, rilpivirine (RPV), and doravirine (DOR). RT mutations confer resistance to NRTIs and NNRTIs (6–9). Biochemical and structural studies help in understanding the molecular mechanisms of drug-resistance mutations. NRTIs are generally DNA chain terminators. The dNTP-binding site and surrounding amino acid residues are mutated to confer resistance to NRTIs. The primary mechanisms of NRTI resistance mutations are steric hindrance such as by M184V/I, discrimination by K65R, and excision of AZT facilitated by thymidine analog mutations (10, 11). NNRTIs bind to a hydrophobic pocket known as the nonnucleoside inhibitor binding pocket (NNIBP), which is adjacent to the polymerase active site. Crystal structures and structure-based approaches have aided the design of new NNRTIs (12–14). The pocket mutations cause NNRTI resistance primarily by steric hindrance and loss of inhibitor–protein

Author contributions: E.A. and K.D. designed research; A.K.S., B.D.W., M.B., S.E.M., and K.D. performed research; K.U., H.N., P.H., and C.P. contributed new reagents/analytic tools; A.K.S., D.S., P.H., C.P., E.A., and K.D. analyzed data; A.K.S., E.A., and K.D. wrote the paper.

The authors declare no competing interest.

This article is a PNAS Direct Submission.

Copyright © 2022 the Author(s). Published by PNAS. This open access article is distributed under Creative Commons Attribution-NonCommercial-NoDerivatives License 4.0 (CC BY-NC-ND).

[1]To whom correspondence may be addressed. Email: kalyan.das@kuleuven.be.

This article contains supporting information online at http://www.pnas.org/lookup/suppl/doi:10.1073/pnas.2203660119/-/DCSupplemental.

Published July 19, 2022.

interactions. Biochemically, mutations at the NNIBP entrance can confer NNRTI resistance by increasing the rate of NNRTI dissociation from NNIBP. The E138K mutation increases the dissociation constant (k_{off}) of RPV by about sevenfold, while the impact of the mutation on k_{on} is negligible (15). Structurally, E138K mutation leads to dissociation of an H-bond between K101 and E138 at the entrance to NNIBP (16).

Structures of HIV-1 RT trapping various functional and conformational states have been determined by X-ray crystallography (17). However, structures of several desired complexes of RT could not be obtained when crystallization or crystal soaking experiments were not successful. The ternary complexes of DOR and RPV with RT/DNA are such examples. The clinically emerging mutations are different for different NNRTIs (18) (https://hivdb.stanford.edu/dr-summary/resistance-notes/NNRTI/). The predominant clinical mutations associated with resistance to rilpivirine are E138K/M184I (or V) (19, 20). The ternary structure of wild-type RT/DNA/RPV and E138K/M184I mutant RT/DNA/RPV can help unravel the roles of these two mutations that are primarily outside the NNIBP and far apart from each other. Our study focuses on finding the molecular mechanism of RPV resistance and visualizing why another second-generation NNRTI DOR is not impacted by the double mutation.

RT is a heterodimer of p66 and p51 subunits with a combined molecular mass of 117 kDa. RT is composed of multiple subdomains and the movement of the subdomains, which is essential for carrying out its functions, makes RT highly flexible in solution. Because of its relatively smaller size and higher flexibility, obtaining atomic-resolution structures of RT and its complexes by single-particle cryo-electron microscopy (cryo-EM) has been challenging. A recent study reported structures of RT/dsRNA/NNRTI (NVP and EFV) minitranscription initiation complexes at resolutions ranging between 2.8 and 3.1 Å (21). In the current study, we are reporting the structures of wild-type and E138K/M184I mutant RT/DNA aptamer (DNA-apt) in complexes with RPV, DOR, and NVP; the resistance mutation E138K is in p51 and M184I is in the p66 subunit, respectively (22). The structures show that the positioning of the DNA with respect to I184 and opening of the NNIBP entrance by E138K mutation may contribute to drug resistance.

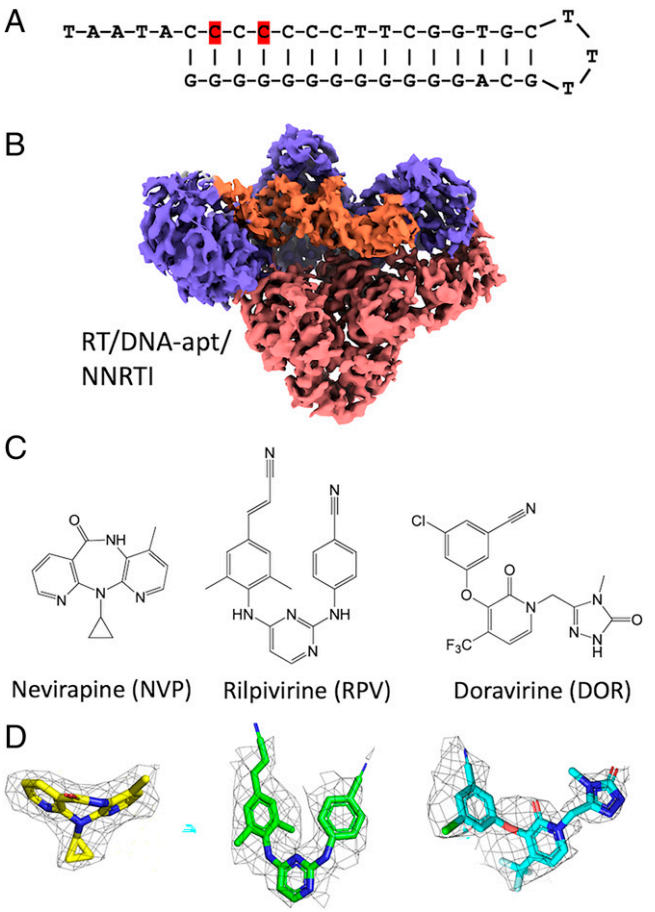

Fig. 1. Cryo-EM structures of RT/DNA/NNRTIs. (*A*) The DNA-apt used in this study to form RT/DNA complex. The aptamers in the wild-type RT/DNA/NNRTI complexes and the mutant RT/DNA/NNRTI complexes have a dTMP and dAMP as the first template overhang, respectively. The modified 2-*O*-methyl dCMP nucleotides at the −2 and −4 positions are highlighted. (*B*) Cryo-EM density map covering the RT/DNA/RPV complex, representing the RT/DNA/NNRTI ternary complex structures. (*C*) Chemical structures of the NNRTI drugs NVP, RPV, and DOR used in the current study. (*D*) The segments of cryo-EM density maps covering the NNRTI drugs NVP, RPV, and DOR; the maps for NVP, RPV, and DOR are contoured at 4.0, 3.2, and 2.2σ, respectively. The stereo views of NNRTI and pocket residues fitted to the experimental density are shown in *SI Appendix*, Fig. 2.

Results

High-Throughput Cryo-EM Structures of RT/DNA/NNRTI Complexes. We have determined six structures of wild-type HIV-1 RT/DNA and M184I/E138K mutant RT/DNA in complexes with the NNRTIs RPV, DOR, and NVP at resolutions ranging from 3.32 to 3.65 Å by single-particle cryo-EM (*SI Appendix*, Table 1). Recently, we trapped an intermediate P-1 complex of RT and determined the cryo-EM structures of the complex with small-molecule fragments bound at a transient P pocket (23). Building on those experiments, we optimized the cryo-EM platform for rapid structure determination of catalytically active RT/DNA and inhibited RT/DNA/NNRTI complexes.

A 38-mer DNA-apt (Fig. 1*A*) binds HIV-1 RT with ∼15 pM affinity, which is ∼100 times higher than a regular dsDNA (24), and was successfully used for structural studies of RT/DNA-apt/dNTP (or analogs) by X-ray crystallography (25, 26). In the current study, RT/DNA-apt complexes were purified using size-exclusion chromatography (SEC) and ascertained to be homogenous by multiangle light scattering and dynamic light scattering (DLS) measurements (*SI Appendix*, Fig. 1*A*). The pure and homogenous RT/DNA samples were incubated with RPV, DOR, or NVP to form respective RT/DNA/NNRTI ternary complexes. The homogeneity of each ternary complex was tested by DLS, and highly reproducible vitreous grids of individual complexes were prepared on Quantifoil holey carbon Au or UltrAuFoil grids using a low sample concentration of ∼0.3 mg/mL. All datasets were collected on a Glacios 200-kV transmission electron microscope (TEM)/Falcon 3 setup. In most cases, fewer than 2,000 micrographs were recorded per complex of which a high percentage were of excellent quality with little to no contamination. The clean micrographs enabled picking good starting sets of particles distributed in well-resolved two-dimensional (2D) classes (*SI Appendix*, Fig. 1*B*) that steered faster processing to high-quality density maps (Fig. 1*B*) including for the bound NNRTIs in each structure (Fig. 1 *C* and *D*). The local resolution maps for all six RT/DNA/NNRTI complexes are in *SI Appendix*, Fig. 1, and the stereo views of inhibitors and NNIBP residues fitting into density maps are shown in *SI Appendix*, Fig. 2.

Structures of RPV, NVP, and DOR in Complex with Wild-Type RT/DNA-Apt. The first structure determined in the series is of wild-type RT/DNA-apt/NVP, which is analogous to the earlier reported crystal structures of RT/DNA/NVP (27) and RT/RNA–DNA/EFV (28). Experimentally, a DNA-apt is used in the

current cryo-EM study of the RT/DNA/NVP complex, whereas RT and DNA were cross-linked in the crystal structure. Both structures align well with root-mean-square deviation (RMSD) of ~0.7 Å for 757 superimposed Cα atoms (*SI Appendix*, Fig. 3); NVP, NNIBP residues, and the cross-linked DNA and aptamer DNA align almost indistinguishably between two structures. The structure comparison shows that using either of two distinct structure determination techniques (X-ray and cryo-EM), with either DNA cross-linking or a DNA-apt, all lead to a very consistent structure of the RT/DNA/NVP complex. For simplicity, hereafter we refer DNA-apt as DNA throughout the text except where different DNAs are directly compared.

The density map for the wild-type RT/DNA/RPV ternary complex (Fig. 2*A*) was obtained at 3.38-Å resolution. The ternary complex superimposes on the crystal structure of the RT/RPV binary complex (29) with RMSD of 1.5 Å for 876 Cα atoms. The conformation and the mode of binding of RPV, however, are not significantly impacted by the binding of DNA (Fig. 2 *B* and *C*). An important structural difference between the binary and ternary complexes of RPV is that upon DNA binding the active-site YMDD motif is lifted toward the DNA by about 2.2 Å at the M184 position. The mutation sites E138 (p51) and M184 (p66) are ~15 Å apart in the RT/DNA/RPV structure (Fig. 2*D*).

The cryo-EM structure of the RT/DNA/DOR ternary complex was determined at 3.65-Å resolution. The structure superimposes on the RT/DOR binary complex (30) with RMSD of 0.99 Å for 793 Cα atoms. The binding of DNA has a significant impact on the primer grip-containing β12−β13−β14 sheet; the primer grip is pushed by about 2 Å to accommodate the DNA (Fig. 2*E*). In contrast, the β6−β10−β9 sheet, which contains the YMDD motif, is less perturbed by the DNA binding; the residue Y181 has an altered rotamer in both RT/DOR and RT/DNA/DOR structures (Fig. 2*F*) when compared to that in other RT/DNA/NNRTI structures. The change in NNIBP in the RT/DNA/DOR complex due to a large shift of the β12−β13−β14 sheet is nonuniform, and consequently DOR is readjusting its rotatable bonds and repositioned (Fig. 2*E*) to adapt to the pocket changes upon DNA binding. In general, the comparisons of ternary and binary complexes of NNRTIs show that DNA binding has different impacts on different NNRTIs. Structurally, RPV and DOR each has at least four rotatable bonds providing torsional freedom which help the NNRTIs to adapt to changes in NNIBP either due to DNA binding and/or pocket modifications (14).

DOR and RPV Ternary Complexes Deviate from the Standard RT/DNA/NNRTI Conformation. Superposition of RT/DNA/NNRTI ternary complex structures shows that the p66 connection, RNase H, and the p51 subunit form a structurally stable core. The polymerase domain, which is composed of fingers, palm, and thumb, has positional differences among the structures (Fig. 3*A*). These differences are rather nonuniform and influenced by the bound NNRTIs. The key structural elements 1) β12−β13−β14 sheet that contains the primer grip and 2) β6−β10−β9 sheet that contains the polymerase active site are known to be involved in the binding of nucleic acid substrates (dsRNA, dsDNA, and RNA–DNA) as well as the NNRTIs. These structural elements align well in the

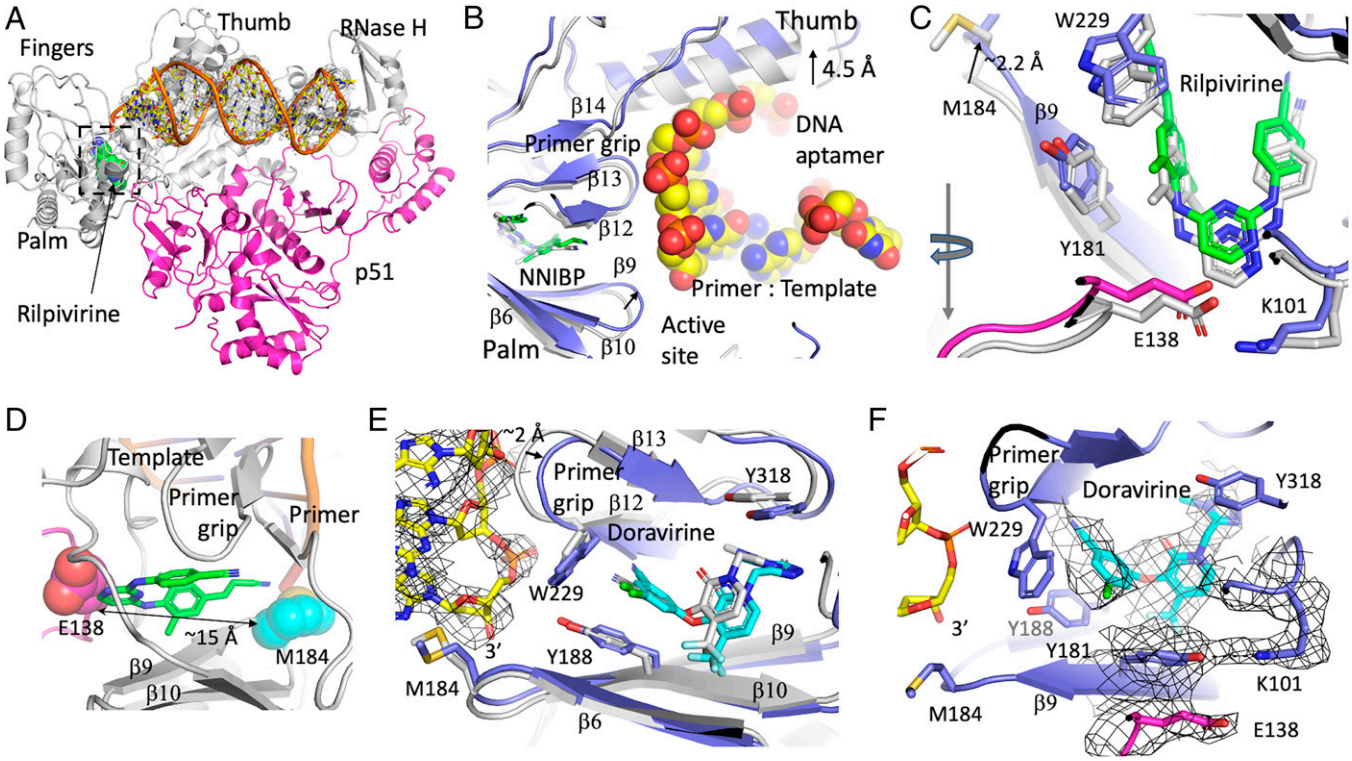

Fig. 2. Structural changes upon DNA binding to RT/RPV and RT/DOR complexes. (*A*) Structure of wild-type HIV-1 RT/DNA/RPV complex; density for the DNA is displayed at 2.5σ. (*B*) A zoomed view of the polymerase active site showing the Cα-superposition of RT/RPV binary complex (PDB ID code 4G1Q; gray) and RT/DNA/RPV ternary complex structures (blue protein, space-filled DNA, and green RPV); 876 Cα atoms superimposed with RMSD of 1.5 Å. There are subtle but important differences between two structures. The tip of the thumb moves outward by ~4.5 Å to accommodate the DNA. (*C*) A zoomed view of the NNIBP region of the superimposed binary and ternary complexes. The $YM_{184}DD$ motif has moved up by ~2 Å in the ternary complex structure. The inhibitor protein interaction and E138 … K101 salt-bridge link are conserved in both structures. (*D*) Relative positioning of two mutation sites E138 (p51) and M184 (p66) in RT/DNA/RPV complex. (*E*) Cα-superposition of RT/DOR binary (PDB ID code 4NCG; gray) and the RT/DNA/DOR ternary complex structures (blue protein, yellow DNA, and cyan DOR); 793 Cα atoms superimposed with RMSD of 0.99 Å. The binding of DNA to RT/DOR repositions the primer grip. (*F*) Cryo-EM density defines the binding of DOR in the RT/DNA/DOR ternary complex. Unlike in the RPV ternary structure, E138 of p51 stacks with the Y181 side chain, which forms a hydrogen bond with K101; the density map is contoured at 2.2σ.

RT/dsRNA minitranscription initiation complexes with or without NNRTIs (21), RT/DNA/NVP (27), and RT/RNA–DNA/EFV (28). In fact, the NNRTI-bound conformation of RT has a close resemblance to the RT/dsRNA transcription initiation state (*SI Appendix*, Fig. 4); only the track of dsRNA is different from that of dsDNA (31). Therefore, the positioning of the primer grip, YMDD motif, and DNA in the RT/DNA/DOR and RT/DNA/RPV complexes was expected to align with those in the RT/DNA/NVP complex. Surprisingly, the DOR- and RPV-bound RT/DNA ternary complex structures have significant perturbation from the standard conformation of the RT/DNA/NNRTI structures; the positioning of the primer grip and the YMDD motif has considerable deviations in the DOR and RPV ternary complexes, respectively (Fig. 3*B*). Unexpectedly, in the RT/DNA/DOR structure, the primer 3′-end is positioned near the active site, which is a contrast to the >5-Å shift of the primer 3′-end in all other RT/DNA/NNRTI structures including RT/DNA/RPV (Fig. 3*C* and *SI Appendix*, Fig. 4*B*).

Current RPV and NVP ternary complex structures superimpose with 0.75-Å RMSD for 757 Cα atoms (Fig. 3*D*). The DNAs follow a common track and the primer grips align; however, the YMDD motifs are positioned differently at ∼4 Å apart. The YMDD-containing β6−β10−β9 sheet in RT/DNA/RPV has skidded significantly from its position in the NVP and DOR ternary complexes (Fig. 3 *E* and *F*). The DNAs in RPV and NVP structures have common, yet not highly superimposable, tracks; the 3′-end nucleotides in RPV and NVP ternary complex structures are ∼2 Å apart. The structures reveal that the binding of second-generation NNRTIs (RPV or DOR) and DNA influence one another, as well as positioning of the key structural elements of RT. These structural differences appear to have roles in developing NNRTI resistance. Like in most RT/NNRTI crystal structures, the p51 E138 side chain forms a salt bridge with the p66 K101 side chain at the NNIBP entrance in NVP and RPV ternary structures. RPV is positioned closer to the NNIBP entrance with a minimum distance of ∼3.5 Å from E138, whereas NVP is positioned deeper in the pocket at a minimum distance of ∼5.4 Å from E138 (Fig. 3*E*). In the DOR ternary complex, the switched conformation of Y181 forms an H-bond with K101 and the E138 side chain stacks with Y181 (Figs. 2*F* and 3*F*).

The DNA Track Is Less Perturbed by DOR than by Other NNRTIs. Biochemically, NNRTIs are known to inhibit the catalytic incorporation of nucleotides (32, 33). The distortion of the catalytic triad or arrest of the primer grip, or most likely the combination of both, contributes to the NNRTI inhibition. An earlier structural study also revealed that NVP binding impedes the binding of dNTP (27). Surprisingly, the DNA track in the DOR complex aligns with that of the catalytically active RT/DNA-apt structure (*SI Appendix*, Fig. 5*A*) (25), which is very different from that in all other RT/DNA/NNRTI ternary complex structures (*SI Appendix*, Fig. 5 *B* and *C*), indicating the possibility that the mechanism of inhibition may be somewhat different for DOR compared to other NNRTIs. The

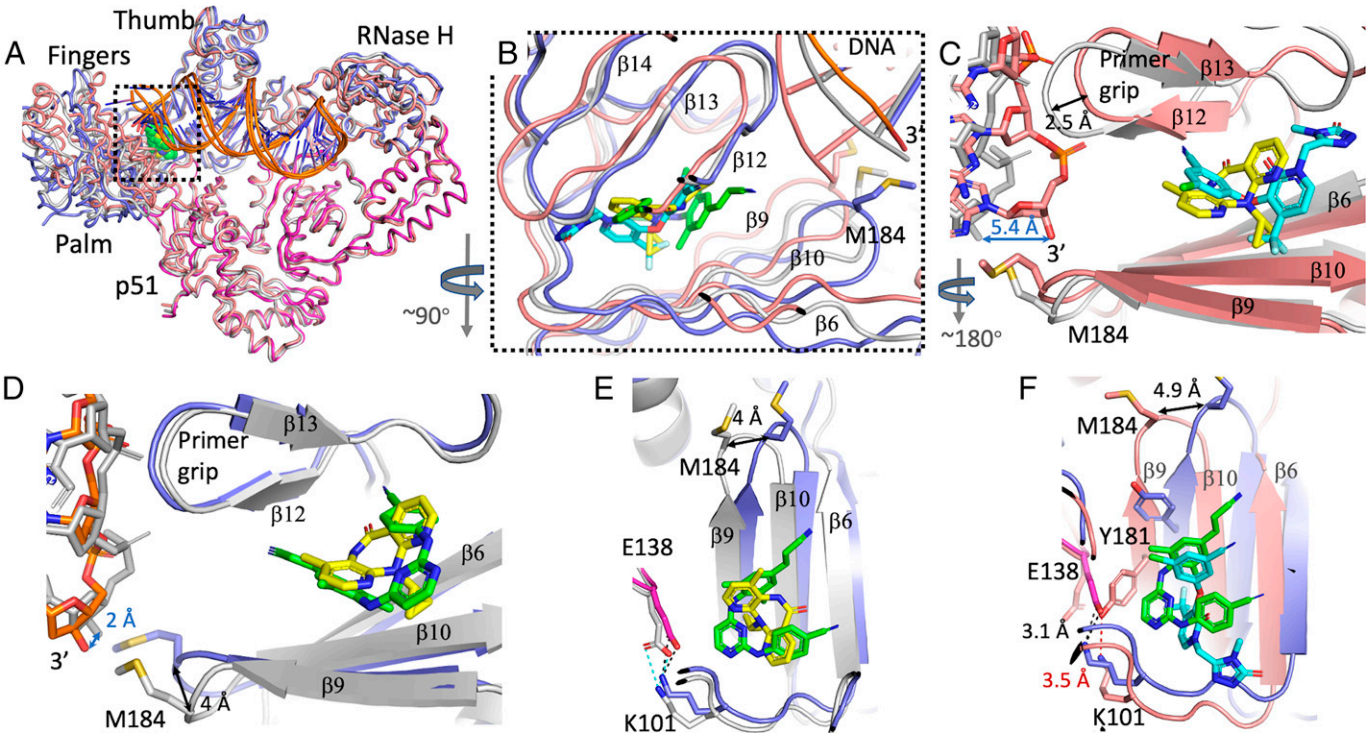

Fig. 3. RT/DNA/RPV and RT/DNA/DOR structures deviate from the standard conformation of RT/DNA/NNRTI complexes represented by RT/DNA/NVP. (*A*) Cα-superposition of HIV-1 RT/DNA/RPV (blue p66, magenta p51), RT/DNA/DOR (salmon), and RT/DNA/NVP (gray). The p51 and p66 connection and RNase H form a structurally stable core; large structural variations are observed for the polymerase domain consisting of fingers, palm, and thumb. Superpositions of these structures with RT/dsRNA/NNRTI complexes are shown in *SI Appendix*, Fig. 4. (*B*) A zoomed-in view of the superimposed structures shows repositioning of the β6−β10−β9 sheet, which contains the YMDD motif, and the β12−β13−β14 sheet, which contains the primer grip; the RT/DNA and NNRTIs are colored blue and green in the RPV complex, salmon and cyan in the DOR complex, and gray and yellow in the NVP complex, respectively. (*C*) Superimposed RT/DNA (salmon)/DOR (cyan) and RT/DNA (gray)/NVP (yellow) structures show that the DNA primer 3′-end has moved by ∼5.4 Å toward the active site in the DOR complex compared to that in NVP complex. Consequently, the primer grip is shifted by ∼2.5 Å in the DOR complex to accommodate the repositioned DNA. (*D*) Superimposed RT (blue)/DNA (orange)/RPV (green) and RT/DNA (gray)/NVP (yellow) structures show a common DNA track; however, the YMDD motif has shifted up by ∼4 Å in the RPV complex. (*E*) A view of the superimposed RPV and NVP structures down the primer grip shows a sliding motion for the β6−β10−β9 sheet upon RPV binding. The K101-E138 salt bridge at about the 7 o'clock position is conserved in both structures; E138 in RPV complex is in magenta. (*F*) The superposition of RTs in RPV (blue p66 and magenta p51 of RT and green RPV) and DOR (salmon RT and cyan DOR) ternary complexes also shows the sliding motion of the β6−β10−β9 sheet in response to the binding of DNA and RPV compared to DOR.

possible modes of inhibition by DOR are as follows: 1) Like for other NNRTIs, the RT/DNA/DOR complex weakens the binding of dNTP at the polymerase active site, 2) an incoming dNTP is bound, however DOR blocks its catalytic incorporation, or 3) one nucleotide is incorporated and the following translocation step is blocked by DOR jamming the primer grip. To investigate the precise mode of DOR inhibition, we attempted the cryo-EM structure of RT/DNA/DOR in the presence of ∼100 times molar excess of dATP as the incoming dNTP. The structure showed no convincing density for dATP at the active site. A dNTP binding is associated with the fingers closing (34); however, the fingers subdomain in our structure remained open, confirming no dATP binding. Our single-nucleotide incorporation assay (*SI Appendix*, Fig. 6), as discussed in the following section, showed no nucleotide incorporation in the presence of DOR. These results confirm that DOR inhibits RT in a fashion analogous to other NNRTIs despite the DNA primer terminal is positioned at the active site in the RT/DNA/DOR complex, i.e., the DNA binds in a nonproductive state in the presence of DOR even though its 3′-end is positioned at the polymerase active site. The track of DNA in the RT/DNA/DOR complex, which is different from that in all other structures, is guided by the repositioning of the primer grip (Fig. 3*C* and *SI Appendix*, Fig. 5). Consequently, the P-1 nucleotide of the DNA that interacts with the primer grip has dipped by ∼4 Å with the primer grip to position the 3′-end at the active site.

E138K and M184I Mutations in Clinical and Biochemical Context. E138K is a nonpolymorphic mutation selected in patients on RPV-containing treatment regimens. It frequently emerges in combination with M184I in patients experiencing virological failure (20). Following the identification of E138K and M184V/I as characteristic RPV-resistance mutations in clinic, studies have been conducted to see the effects of the mutations in cell-based assays and at the enzyme level. Enzymatically, E138K/M184I RT has a moderate increase in resistance to RPV (15, 35). Phenotypic assays have shown that E138K in the p51 subunit alone decreases RPV susceptibility by about 2.4-fold while the coexistence of M184I in p66 further brings the susceptibility down to approximately fivefold (36); M184I/V mutation alone, however, does not alter RPV susceptibility. M184I/V is a nucleoside-resistance mutation, which negatively affects the RT replication capacity as shown earlier by steady-state kinetic experiments; the Michaelis constant (K_m) was 14.6 for the mutant vs. 5.6 μM for the wild-type enzyme (37). The decrease in enzyme functionality, however, gets compensated by E138K in p51 which restores the K_m for dNTP to a value comparable to the wild-type enzyme. Thus, the clinical selection of E138K and M184I mutations seems to play a dual role—conferring RPV resistance and improving the viral fitness as a compensatory mutation. The effect of E138K mutation on DOR susceptibility has been also studied. E138K has not been selected against DOR in clinic or shown to affect DOR susceptibility to a noticeable degree in vitro (38, 39). DOR and RPV are shown to have complementary resistance mutation profiles (40). The published antiviral data and the enzymatic assay results carried out in this study are listed in Table 1.

To investigate the inhibitory effects of NVP, RPV, and DOR on the wild-type and E138K/M184I RTs, we employed two separate sets of biochemical assays. Inhibition assay to determine IC_{50} values (50% inhibitory concentration) for the inhibitors on the wild-type and (E138K/M184I) RTs were carried out using EnzChek Reverse Transcriptase Assay Kit (Thermo Fisher Scientific) (Table 1 and *SI Appendix*, Table 2). Our assay shows that NVP inhibits both wild-type and the mutant RT at a comparable IC_{50}; however, reduced susceptibility for NVP by the E138K/M184I mutant RT of HIV-1 subtype C has been previously shown in a phenotypic assay (9). For both RPV and DOR, our assay results show a moderate decrease in susceptibility by E138K/M184I RT over the wild-type RT with a resistance fold change of ∼2.3 and 2.4, respectively (Table 1).

In parallel, we have also performed a gel-based single-nucleotide incorporation assay (42) to assess the effect of NVP, RPV, and DOR on DNA polymerization by RT. All three NNRTIs inhibit DNA polymerization by wild-type and E138K/M184I RTs in a dose-dependent manner with the mutant RT showing slightly reduced susceptibility toward all three inhibitors (*SI Appendix*, Fig. 6). Our assay results follow the observed trend in earlier studies. The difference between the inhibition data from two assays that we performed on same RT samples in the current study, which is also reflected in the published data (Table 1), may be attributed to the relative sensitivity and experimental protocol differences.

Structures of E138K/M184I Mutant RT/DNA in Complexes with RPV, NVP, and DOR. We determined the cryo-EM structures of E138K/M184I mutant RT/DNA in complexes with NVP, RPV,

Table 1. Inhibitory activity of NVP, RPV, and DOR against wild-type and E138K/M184I (or V) HIV-1 RT and viruses

	IC_{50}, nM		
	NVP	RPV	DOR
RT			
Wild type	130 ± 10	3.9 ± 0.4	11 ± 1
E138K/M184I*	88 ± 17 (0.7)	8.9 ± 0 (2.3)	26 ± 1 (2.4)
Published antiviral resistance data (fold resistance)			
Fold resistance by E138K/M184I (36)	0.7	2.5	
Fold resistance by E138K/M184V (36)	0.9	2.0	
Fold resistance by E138K/M184I (9)	5.2	4.5	
Fold resistance by E138K/M184V (9)	6.2	3.0	
Fold resistance by E138K/M184I (40)		∼5.5	∼2.0
Fold resistance by E138K/M184V (40)		∼6.5	∼4.2
Fold resistance by E138K/M184I (41)		3.1	
Fold resistance by E138K/M184I (41)		1.3	
Fold resistance by E138K/M184I (35)		4.3	

*Values in parentheses represent resistance fold change with respect to the wild-type RT. SD for each measurement is indicated.

and DOR at 3.38-, 3.45-, and 3.58-Å resolution, respectively (*SI Appendix*, Table 1). The (E138K/M184I) RT/DNA/NNRTI structures align well with their respective wild-type RT/DNA/NNRTI structures, suggesting that the mutations have no significant long-range impacts; 879 Cα atoms align with 0.62-Å RMSD for the RPV complex, 906 Cα atoms aligned with 0.69-Å RMSD for DOR complexes, and 838 Cα atoms aligned with 0.64-Å RMSD for NVP complexes. Two mutation sites, E138K at the entrance to NNIBP and M184I of YMDD motif, are ∼15 Å apart in RPV-, ∼13 Å in NVP-, and ∼11 Å in DOR-bound ternary complexes; this distance is ∼11 Å in the active RT/DNA complex with no bound NNRTI. An earlier structural study had shown that the loss of a salt bridge between E138 and K101 in the E138K mutant is the primary contributor to NNRTI resistance (16). The current cryo-EM density maps of wild-type and mutant RT/DNA/NVP and RT/DNA/RPV complexes show the loss of the salt bridge by the E138K mutation (Fig. 4 *A* and *B*); RPV is positioned closer to the NNIBP entrance. The pocket entrance in the DOR-bound structure is least influenced by the E138K mutation. The aromatic side chain of Y181 that blocks the entrance (Fig. 3*F*) in the wild-type complex loses the H-bond with K101 in the mutant complex; however, the Y181 side chain still blocks the NNIBP entrance, which may prevent faster dissociation of DOR from NNIBP (Fig. 4*C*).

M184I/V is an NRTI-resistant mutation that reduces the susceptibility of L-nucleotide analogs lamivudine (3TC) and emtricitabine (FTC) to HIV (43, 44). Kinetic studies and crystal structures have revealed that the 3TCTP (or FTCTP) binds M184I/V RT in a nonproductive mode with lower affinity when compared to dCTP (34, 45, 46). However, it was not clear how M184I/V mutation contributes to NNRTI resistance. Both E138K and M184I mutations have mild impacts on NNIBP residues, the track of DNA, and the positioning of the YM(I)DD loop in the RPV-bound structures when compared with respective wild-type complexes (Fig. 5 *A* and *B*). The cyanovinyl group attached to the dimethylanilino ring of RPV has flipped in the mutant structure when compared to the wild-type complex (Fig. 5*C*); the experimental density and relative positioning of the dimethylanilino ring and surrounding residues confirm the flipped orientation of the cyanovinyl group. The adaptability of the cyanovinyl group and its interactions with RT are critical for the binding of RPV and for retaining its potency against several NNRTI-resistant mutations (14, 29). The relative positioning of the I184 side chain with respect to the DNA primer 3′-end nucleotide is distinct in the RPV complex when compared to that in the mutant RT/DNA/DOR (Fig. 5*D*) and RT/DNA/NVP (Fig. 5*E*) structures. The I184 side chain and the sugar-phosphate backbone of the primer 3′-end nucleotide are stacked (Fig. 5*F*). It is clear from the structures that in a dynamic state in which RT slides over a nucleic acid substrate (47), the YM(I)DD motif in the RPV complex would respond differently than that in other

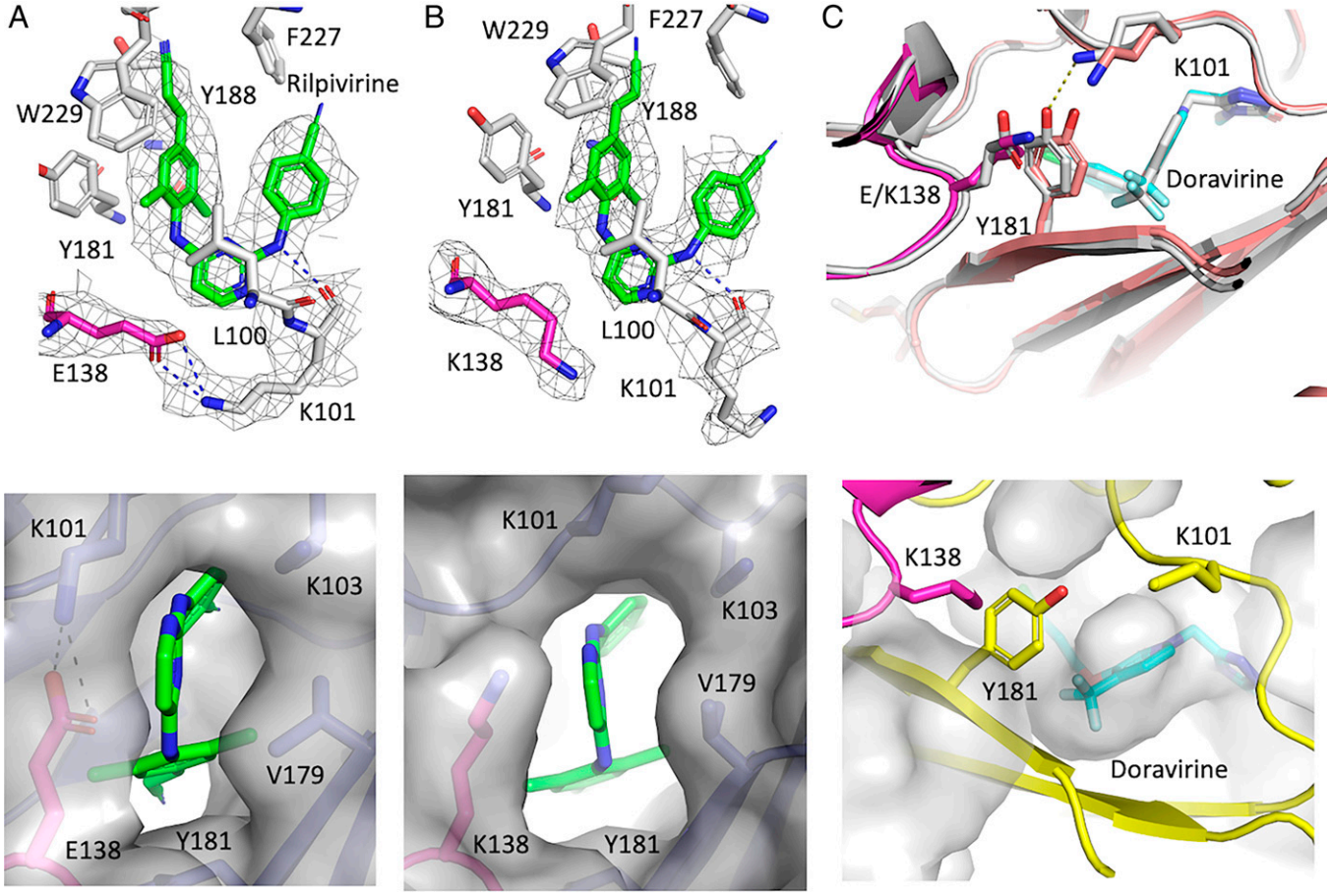

Fig. 4. E138K mutation at the NNIBP entrance in RPV and DOR ternary complexes. RPV and surrounding residues in wild-type (*A*) and M184I/E138K mutant RT (*B*) ternary complexes; both maps were displayed at 3.0σ contour. The bottom panels show the molecular surfaces at the NNIBP entrance of respective structures. The cryo-EM density is shown for RPV, E/K138 (p51), and K101. The loss of the H-bond between E138 and K101 by E138K mutation opens the entrance to the pocket. (*C*) A comparison of the pocket entrances in the wild-type and E138K/M184I mutant RT/DNA/DOR complexes reveals no significant impact of the mutations at the NNIBP entrance; the entrance is covered by the Y181 side chain in both RT/DNA/DOR structures. The molecular surface of DOR in the bottom panel gives an impression of the entrance blocking by Y181.

NNRTI ternary complexes. In the RPV complex, I184 and the DNA face each other, which may restrict the motion of YM(I)DD loop. However, in the NVP and DOR complexes, the YM(I)DD motif would be able to move up and down like a springboard, which is also the natural motion of the loop for carrying out dNTP binding, DNA polymerization, and translocation. The ability of RPV to adapt to the changes around it (14) would help compensate for the potential impact from the M184I mutation alone; however, an unblocked NNIBP entrance caused by the E138K mutation would help in increasing the rate of dissociation of RPV. These observations support the earlier studies which showed that viruses containing only M184I would retain full susceptibility toward RPV whereas the E138K/M184I mutant reduces RPV susceptibility by lowering RPV's equilibrium binding affinity to the mutant RT (15, 36).

Discussion

The structural adaptability of the second-generation NNRTIs such as RPV and DOR helps the drugs overcome the impacts of common NNRTI-resistance mutations such as Y181C, which is deleterious to NVP. The binding pocket is predominantly hydrophobic, and so are the NNRTIs. Biochemically, the impacts of E138K or E138K/M184I mutations on NNRTIs are rather low in our assays, which are in agreement with prior studies. The current cryo-EM structures of the NNRTI ternary complexes show that an open pocket entrance and the relative positioning of I184 with respect to the DNA substrate in the RPV-bound structure appear to contribute to RPV resistance by E138K/M184I mutations. Because of the weak effects on inhibition by E138K/M184I mutations observed in antiviral and biochemical assays (Table 1) it has been difficult to strongly correlate those with RPV treatment failure in the clinic. Interestingly, the structural features of the RT/DNA/RPV complex near the mutation sites are significantly different from that in other RT/DNA/NNRTI structures. While the structural differences may help explain the distinct impacts of the mutations on RPV, it is expected that in general the structures relate more closely to enzymatic data than to clinical observations. Based on its location away from the polymerase active site, E138K may be selected more easily as an RPV-resistance mutation compared to other pocket mutations. Emergence of M184I (or V) in an E138K background apparently does not add a fitness cost because the later is a compensatory mutation when M184I emerges first as an NRTI-resistance mutation. This reasoning may suggest that HIV-1 can develop E138K/M184I mutations at little to no fitness cost compared to other RPV-resistance mutations even though the resistance level to RPV is low. Additional innovative experiments to find a better correlation of the enzymatic/antiviral data with the clinical findings may further elucidate the impacts of the mutations.

A striking difference of the RT/DNA/DOR complex is that the track of DNA is less influenced by the binding of DOR. The size and shape of the NNRTIs influence the arrangement of the key structural elements—YMDD motif, primer grip, track of DNA, the pocket entrance, etc. The relative distance between the two mutation sites E138K (p51) and M184I (p66) also varies among RT/DNA/NNRTI ternary complex structures; the distance between the two Cα positions is maximum in the RPV

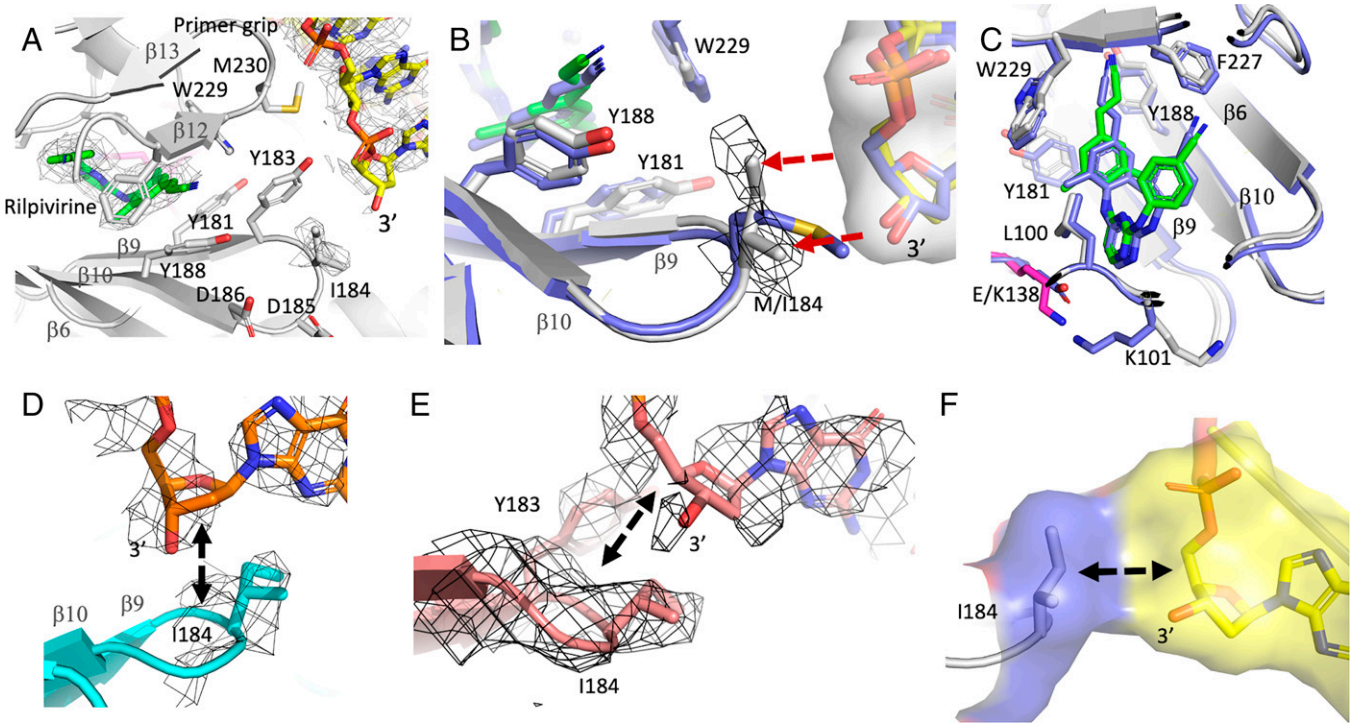

Fig. 5. Relative positioning of the mutated I184 residue with respect to the DNA primer 3′-end is distinct in the RPV-bound complex when compared to DOR and NVP ternary complexes. (*A*) The NNIBP and polymerase active site in M184I/E138K mutant RT (gray)/DNA (yellow)/RPV (green) structure; the cryo-EM density for I184 and DNA is contoured at 2.0σ. (*B*) Superposition of the wild-type RT/DNA/RPV structure (blue) on the mutant RT (gray)/DNA (yellow)/RPV (green) complex shows that the β-branched rigid side chain of I184 compared to a more flexible M184 side chain is locked against the DNA primer 3′-end nucleotide; the density map for I184 is contoured at 2.0σ. (*C*) The binding mode of RPV (green) in the mutant RT (gray)/DNA (yellow)/RPV ternary complex has its cyanovinyl group flipped when compared to the wild-type RT/DNA/RPV (blue) complex. (*D*) Relative positioning of the DNA primer 3′-end with respect to the YM(I)DD motif in the (M184I/E138K) RT (cyan)/DNA (orange)/DOR structure. (*E*) Relative positioning of the DNA primer end with respect to the YM(I)DD motif in the (M184I + E138K) RT/DNA (salmon)/NVP structure. The displayed sections of the cryo-EM densities in panels *D* and *E* are contoured at 2.0σ. (*F*) The molecular surface showing the extensive interaction between I184 and the backbone of the primer 3′-end nucleotide in the (M184I/E138K) RT/DNA/RPV ternary complex.

complex, whereas the distance is not altered in the DOR complex when compared to the polymerase active RT/DNA complex. This result suggests that large structural deviations from the RT/DNA elongation complex induced by the binding of an NNRTI may lead to structural vulnerabilities that are susceptible to resistance mutations. Therefore, routine analysis of the structural features of NNRTI-inhibited RT/DNA (or RNA–DNA) elongation complexes may be worthwhile for effective design of NNRTIs. The optimized single-particle cryo-EM protocol outlined in this study will help overcome the limitation of growing crystals of desirable wild-type and mutant HIV-1 RT/DNA/NNRTI complexes. The single-particle cryo-EM technique has been very powerful in obtaining new structures of challenging macromolecule complexes in recent years. The current study provides one of the few examples of how the cryo-EM technique can be optimized for rapid structure determination to aid drug design.

Materials and Methods

RT Double-Mutant Construction. To create the HIV-1 RT double mutant containing E138K and M184I mutations in p51 and p66 domains, respectively, two separate pETDuet-1 vectors harboring p51 and p66 coding segments were used. The two domains constitute an RT construct (RT139A) as reported previously (48). Overlapping primers (p51-For-E138K-ATTAACAATAAAACTCCCGGGATC and p51-Rev-E138K-GGAGTTTTATTGTTAATGCTAGGGAT; p66-For-M184I-ATTTATCAATATATAGATGACTTGT and p66-Rev-M184I-CATACAAGTCATCTATATATTGA) were used in PCR to introduce the desired nucleotide changes. One microliter of each plasmid at ∼1.5 ng/μL concentration was used as template and the reactions were carried out with Q5 High-Fidelity DNA Polymerase (New England Biolabs). PCR products were gel-purified and successful mutagenesis was confirmed by sequencing (Macrogen). The amplified plasmid containing the mutated p66 was double-digested with NdeI and XhoI restriction enzymes (New England Biolabs), gel-purified, and cloned into MCS-2 of the pETDuet-1 vector predigested with the same set of restriction enzymes and carrying mutated p51 domain in MCS-1. Hereafter we refer to this double mutant as RT600.

RT139A and RT600 Expression, Purification, and Complexes of RT/38-mer Aptamer DNA. Expression and purification of RT139A containing the I63C mutation was carried out as described previously (48). Briefly, the protein expression in *Escherichia coli* BL21-CodonPlus (DE3)-RIL cells (Agilent Technologies) was induced with 1 mM isopropyl β-D-1-thiogalactopyranoside (IPTG) and continued for 3 h at 37 °C. Cell disruption was achieved by sonication (Branson Sonifier SFX250) and the soluble fraction was subjected to immobilized metal affinity purification using a 5-mL Ni-NTA column (GE Healthcare) connected to an FPLC system (GE Healthcare). The 6xHis tag was cleaved from the N terminus of p51 using a 1:10 mass ratio of HRV14 3C protease to RT by overnight treatment on ice. The protein was further purified by anion-exchange chromatography on a Mono-Q column (GE Healthcare).

Expression and purification of RT600 was carried out in a similar way as with RT139A except that the 6x-His tag on the p51 N terminus was not cleaved. The Mono-Q purified RTs were stored in a buffer containing 10 mM Tris·HCl, pH 8.0, and 75 mM NaCl at −80 °C for future use.

We used two 38-mer DNA-hairpin aptamers in this study, 5′-TAATTCC CCCCCTTCGGTGCTTTGCACCGAAGGGGGGG-3′ (T overhang) and 5′-TAATACCCCCCC TTCGGTGCTTTGCACCGAAGGGGGGG-3′ (A overhang), to complex with RT139 and RT600, respectively. The aptamers were purchased from Integrated DNA Technologies. RT/DNA-apt complexes were prepared following earlier described protocol (23, 25). Briefly, the aptamer pellet was resuspended in a buffer containing 10 mM Tris, pH 8.0, 50 mM NaCl, and 1 mM ethylenediaminetetraacetic acid (EDTA) and added to the protein in 1.2:1 molar ratio. The individual complexes were incubated over ice for 1 h and purified by SEC using a Superdex 200 10/300 GL column (GE Healthcare) preequilibrated in a buffer containing 10 mM Tris·HCl, pH 8.0, and 75 mM NaCl. The RT139A/DNA-apt and RT600/DNA-apt complex formation were confirmed by optical density (OD) OD_{260}:OD_{280} measurement of ∼0.95 and shift in the SEC elution profile.

Biochemical Assay. The RT inhibition assay was carried out using a Cy5-fluorophore–labeled 17-mer primer (5′- Cy5-CAGGAAACAGCTATGAC-3′) and a template (5′- GGGTGTCATAGCTGTTTCCTG-3′) following a published protocol (42). Each 20-μL enzymatic reaction mixture containing 125 nM primer–template was prepared in 50 mM Tris·HCl, pH 8.3, 3 mM $MgCl_2$, 10 mM dithiothreitol (DTT), and 1 μM dATP. The NNRTIs RPV, DOR, and NVP were used at indicated concentrations (*SI Appendix*, Fig. 4), and 0.006 μg of RT was added per 1-μL reaction. The primer and template were preannealed at 1:2 molar ratio by heating to 95 °C and cooling down to room temperature. The reaction mixture without dATP was preincubated at 37 °C for 20 min. The reaction was initiated by adding the dATP and quenched after 1 min by adding a double volume of quenching buffer (90% formamide, 50 mM EDTA, and 0.05% orange G) and heating at 95 °C for 5 min. The samples were separated on a 1-mm 15% denaturing polyacrylamide gel, and gel bands were visualized using the Typhoon FLA 9500 imaging system (GE Healthcare). The images were processed using ImageQuant TL v8.1.0.0 (GE Healthcare).

PicoGreen RT Assay. The RT assay was performed with the EnzCheck Reverse Transcriptase Assay kit (Molecular Probes, Invitrogen), as described by the manufacturer. The assay is based on the dsDNA quantitation reagent PicoGreen. This reagent shows a pronounced increase in fluorescence signal upon binding to dsDNA or RNA/DNA heteroduplexes. Single-stranded nucleic acids generate only minor fluorescence signal enhancement when a sufficiently high dye to base pair ratio is applied (49). This condition is met in the assay. Five μL of 1 mg/mL poly(rA) template of ∼350 bases long was annealed with 5 μL of a 50 μg/mL oligo(dT)16 primer at a molar ratio of 1:1.2 (60 min at room temperature). The annealed template/primer was then diluted 180-fold in polymerization buffer (60 mM Tris·HCl, pH 8.1, 60 mM KCl, 8 mM $MgCl_2$, 13 mM DTT, and 100 μM dTTP) and 17 μL of this RNA/DNA was brought into each well of a 96-well flat-black plate. To test the RT inhibition, 3 μL of compound in dimethyl sulfoxide (DMSO) was added to each well before the addition of RT enzyme solution. Control wells without compound contained the same amount of DMSO. Five microliters of RT enzyme solution, diluted to a suitable concentration in the enzyme dilution buffer (50 mM Tris·HCl, pH 7.5, 20% glycerol, and 1 mM DTT) was added. The reactions were incubated at 25 °C for 40 min and then stopped by adding 2 μL of 200 mM EDTA. Heteroduplexes were then detected by addition of 173 μl 0.73 μM PicoGreen. Signals were read using an excitation wavelength of 490 nm and emission detection at 523 nm in a spectrofluorometer (Safire 2, Tecan). The results (summarized in Table 1 and detailed in *SI Appendix*, Table 2) are expressed as relative fluorescence, i.e., the fluorescence signal of the reaction mix with compound divided by the signal of the same reaction mix without compound.

Inhibitor Complex Preparation for Cryo-EM. Inhibitor stocks (NVP, RPV, and DOR) were prepared in 100% DMSO and diluted down to ∼0.5 to 1 mM working stocks in buffer containing 10 mM Tris·HCl, pH 8.0, and 75 mM NaCl immediately prior to use. Protein samples stored in 10 mM Tris·HCl, pH 8.0, and 75 mM NaCl at −80 °C were thawed on ice, diluted down to 0.3 mg/mL (2.3 μM), and the inhibitors were added at a 1:1.2 protein:inhibitor molar ratio. The mixtures were allowed to incubate over ice for 1 h to ascertain the formation of the respective complexes and each complex spun down in a tabletop centrifuge at 16,000 × *g* for 10 min that settles any aggregates to the bottom; the sample on top was used for preparing cryo-EM grids. To find if dNTP can bind the RT/DNA/DOR complex, ∼100× molar excess dATP was added to the 1-h-incubated sample of the RT/DNA/DOR complex.

Cryo-EM Grid Preparation and Data Collection. The cryo-EM grids of RT139A/DNA-apt and RT600/DNA-apt in complexes with RPV, NVP, and DOR were prepared on Quantifoil R1.2/1.3 gold mesh grids with either holey carbon or UltrAuFoil films (Quantifoil). The holey carbon film grids were precleaned in chloroform for 2 to 3 h at room temperature and allowed to dry overnight prior to use, and the ones with UltrAuFoil film were used without any cleaning. The grids were glow-discharged for 45 s at 25 mA with the chamber pressure set at 0.3 mbar (PELCO easiGlow; Ted Pella). The grids were mounted in the sample chamber of a Leica EM GP set at 8 °C and 95% relative humidity. Optimized grids were obtained by applying 3 μL of the sample at 0.3 mg/mL, incubating for 30 s, back-blotting for 14 s using Whatman grade 1 filter paper, and plunge-freezing in liquid ethane at −172 °C. The prepared grids were then clipped and

mounted on a 200-kV Glacios TEM (Thermo Fisher Scientific) equipped with autoloader and Falcon 3 direct electron detector as installed in the K.D. laboratory.

Cryo-EM datasets were collected from the vitrified hydrated grids in counting mode on the Glacios TEM using EPU software version 2.9.0 (Thermo Fisher Scientific). The movies were collected at a nominal magnification of 150,000×, yielding a pixel size of 0.97 Å. Each movie was collected with 40 frames, where each frame received ∼1 e/Å^2, for a total dose of 40 e/Å^2, and subsequently written as a gain-corrected MRC file. Data collection statistics are listed in *SI Appendix*, Table 1.

Cryo-EM Data Processing. Individual movie frames were motion-corrected and aligned using MotionCor2 (50) as implemented in the Relion 3.1 package (51) and the contrast transfer function (CTF) parameters were estimated by CTFFIND-4 (52). The particles were automatically picked using the reference-free Laplacian-of-Gaussian routine in Relion 3.1. The picked particles were initially classified as three-dimensional (3D) classes which proved to be more efficient than initial 2D classification. The 3D classification generated a distinct single class of particles with meaningful map connectivity and highest estimated resolution compared to other classes. The particles in the good 3D class were reextracted and subjected to 2D and 3D classifications. No additional 3D classes representing RT/DNA or RT/NNRTI states or alternate conformation of RT/DNA/NNRTI were observed. The final set of particles for each RT/DNA/NNRTI complex was used to calculate gold-standard auto-refined maps, which were further improved by B polishing and CTF refinement. All data processing was carried out using Relion 3.1.

Model Building. RT/DNA-apt crystal structure (Protein Data Bank [PDB] ID code 5HP1) was used as the starting model for fitting the atomic structure to the density map of RT/DNA-apt/NVP complex. The RT/DNA-apt/NVP structure was subsequently used as the template for building other structures reported in this study. Manual model fitting to the density map was carried out in Coot (53) followed by real-space model refinement using Phenix 1.19 (54). The inhibitor model and restrain files were obtained from PDB. All structure figures were prepared using PyMOL (https://pymol.org/2/) and Chimera (55).

Data Availability. The density maps and atomic coordinates for the structures reported in this paper have been deposited in the Electron Microscopy Databank (EMDB) and Protein Data Bank (PDB), respectively. The accession codes are EMD-14457 (56) and 7Z24 (57) for wild-type RT/DNA/NVP; EMD-14458 (58) and 7Z29 (59) for E138K/M184I mutant RT/DNA/NVP; EMD-14462 (60) and 7Z2D (61) for wild-type RT/DNA/RPV; EMD-14463 (62) and 7Z2E (63) for E138K/M184I mutant RT/DNA/RPV; EMD-14465 (64) and 7Z2G (65) for wild-type RT/DNA/DOR; and EMD-14466 (66) and 7Z2H (67) for E138K/M184I mutant RT/DNA/DOR.

ACKNOWLEDGMENTS. We acknowledge the contributions of our dear colleague Sergio E. Martinez, who passed away recently, to studies of macromolecule structures and structure-based drug design, including the research published in this paper. This study was supported by Rega Virology and Chemotherapy internal grants to K.D., and E.A. acknowledges NIH Grant R01 AI027690 for support.

Author affiliations: [a]Laboratory of Virology and Chemotherapy, Rega Institute for Medical Research, KU Leuven, 3000 Leuven, Belgium; [b]Department of Microbiology, Immunology and Transplantation, KU Leuven, 3000 Leuven, Belgium; [c]Laboratory of Medicinal Chemistry, Rega Institute for Medical Research, KU Leuven, 3000 Leuven, Belgium; [d]Department of Pharmaceutical and Pharmacological Sciences, KU Leuven, 3000 Leuven, Belgium; [e]Center for Advanced Biotechnology and Medicine, Rutgers University, Piscataway, NJ 08854; and [f]Department of Chemistry and Chemical Biology, Rutgers University, Piscataway, NJ 08854

1. E. J. Arts, D. J. Hazuda, HIV-1 antiretroviral drug therapy. *Cold Spring Harb. Perspect. Med.* **2**, a007161 (2012).
2. M. S. Saag *et al.*, Antiretroviral drugs for treatment and prevention of HIV infection in adults: 2020 recommendations of the International Antiviral Society-USA Panel. *JAMA* **324**, 1651–1669 (2020).
3. C. Flexner, HIV drug development: The next 25 years. *Nat. Rev. Drug Discov.* **6**, 959–966 (2007).
4. A. Engelman, P. Cherepanov, The structural biology of HIV-1: Mechanistic and therapeutic insights. *Nat. Rev. Microbiol.* **10**, 279–290 (2012).
5. E. De Clercq, Strategies in the design of antiviral drugs. *Nat. Rev. Drug Discov.* **1**, 13–25 (2002).
6. K. Das, E. Arnold, HIV-1 reverse transcriptase and antiviral drug resistance. Part 2. *Curr. Opin. Virol.* **3**, 119–128 (2013).
7. M. E. Cilento, K. A. Kirby, S. G. Sarafianos, Avoiding drug resistance in HIV reverse transcriptase. *Chem. Rev.* **121**, 3271–3296 (2021).
8. L. Menéndez-Arias, M. Alvarez, Antiretroviral therapy and drug resistance in human immunodeficiency virus type 2 infection. *Antiviral Res.* **102**, 70–86 (2014).
9. A. E. Basson *et al.*, Impact of drug resistance-associated amino acid changes in HIV-1 subtype C on susceptibility to newer nonnucleoside reverse transcriptase inhibitors. *Antimicrob. Agents Chemother.* **59**, 960–971 (2015).
10. K. Das *et al.*, Structural basis for the role of the K65R mutation in HIV-1 reverse transcriptase polymerization, excision antagonism, and tenofovir resistance. *J. Biol. Chem.* **284**, 35092–35100 (2009).
11. W. A. Scott, Structures of reverse transcriptase pre- and post-excision complexes shed new light on HIV-1 AZT resistance. *Viruses* **3**, 20–25 (2011).
12. W. L. Jorgensen *et al.*, Computer-aided design of non-nucleoside inhibitors of HIV-1 reverse transcriptase. *Bioorg. Med. Chem. Lett.* **16**, 663–667 (2006).
13. C. Zhuang, C. Pannecouque, E. De Clercq, F. Chen, Development of non-nucleoside reverse transcriptase inhibitors (NNRTIs): Our past twenty years. *Acta Pharm. Sin. B* **10**, 961–978 (2020).
14. K. Das *et al.*, Roles of conformational and positional adaptability in structure-based design of TMC125-R165335 (etravirine) and related non-nucleoside reverse transcriptase inhibitors that are highly potent and effective against wild-type and drug-resistant HIV-1 variants. *J. Med. Chem.* **47**, 2550–2560 (2004).
15. K. Singh *et al.*, Biochemical mechanism of HIV-1 resistance to rilpivirine. *J. Biol. Chem.* **287**, 38110–38123 (2012).
16. J. Ren *et al.*, Structural insights into mechanisms of non-nucleoside drug resistance for HIV-1 reverse transcriptases mutated at codons 101 or 138. *FEBS J.* **273**, 3850–3860 (2006).
17. K. Das, E. Arnold, HIV-1 reverse transcriptase and antiviral drug resistance. Part 1. *Curr. Opin. Virol.* **3**, 111–118 (2013).
18. N. Sluis-Cremer, M. A. Wainberg, R. F. Schinazi, Resistance to reverse transcriptase inhibitors used in the treatment and prevention of HIV-1 infection. *Future Microbiol.* **10**, 1773–1782 (2015).
19. C. J. Cohen *et al.*; ECHO Study Group; THRIVE Study Group, Efficacy and safety of rilpivirine (TMC278) versus efavirenz at 48 weeks in treatment-naive HIV-1-infected patients: Pooled results from the phase 3 double-blind randomized ECHO and THRIVE Trials. *J. Acquir. Immune Defic. Syndr.* **60**, 33–42 (2012).
20. L. Rimsky *et al.*, 96-Week resistance analyses of rilpivirine in treatment-naive, HIV-1-infected adults from the ECHO and THRIVE Phase III trials. *Antivir. Ther.* **18**, 967–977 (2013).
21. B. Ha *et al.*, High-resolution view of HIV-1 reverse transcriptase initiation complexes and inhibition by NNRTI drugs. *Nat. Commun.* **12**, 2500 (2021).
22. H. T. Xu *et al.*, Subunit-selective mutational analysis and tissue culture evaluations of the interactions of the E138K and M184I mutations in HIV-1 reverse transcriptase. *J. Virol.* **86**, 8422–8431 (2012).
23. A. K. Singh *et al.*, Sliding of HIV-1 reverse transcriptase over DNA creates a transient P pocket–Targeting P-pocket by fragment screening. *Nat. Commun.* **12**, 7127 (2021).
24. J. J. DeStefano, J. V. Cristofaro, Selection of primer-template sequences that bind human immunodeficiency virus reverse transcriptase with high affinity. *Nucleic Acids Res.* **34**, 130–139 (2006).
25. M. T. Miller, S. Tuske, K. Das, J. J. DeStefano, E. Arnold, Structure of HIV-1 reverse transcriptase bound to a novel 38-mer hairpin template-primer DNA aptamer. *Protein Sci.* **25**, 46–55 (2016).
26. K. Das *et al.*, Conformational states of HIV-1 reverse transcriptase for nucleotide incorporation vs pyrophosphorolysis-binding of foscarnet. *ACS Chem. Biol.* **11**, 2158–2164 (2016).
27. K. Das, S. E. Martinez, J. D. Bauman, E. Arnold, HIV-1 reverse transcriptase complex with DNA and nevirapine reveals non-nucleoside inhibition mechanism. *Nat. Struct. Mol. Biol.* **19**, 253–259 (2012).
28. M. Lapkouski, L. Tian, J. T. Miller, S. F. J. Le Grice, W. Yang, Complexes of HIV-1 RT, NNRTI and RNA/DNA hybrid reveal a structure compatible with RNA degradation. *Nat. Struct. Mol. Biol.* **20**, 230–236 (2013).
29. K. Das *et al.*, High-resolution structures of HIV-1 reverse transcriptase/TMC278 complexes: Strategic flexibility explains potency against resistance mutations. *Proc. Natl. Acad. Sci. U.S.A.* **105**, 1466–1471 (2008).
30. B. Côté *et al.*, Discovery of MK-1439, an orally bioavailable non-nucleoside reverse transcriptase inhibitor potent against a wide range of resistant mutant HIV viruses. *Bioorg. Med. Chem. Lett.* **24**, 917–922 (2014).
31. K. Das, S. E. Martinez, J. J. DeStefano, E. Arnold, Structure of HIV-1 RT/dsRNA initiation complex prior to nucleotide incorporation. *Proc. Natl. Acad. Sci. U.S.A.* **116**, 7308–7313 (2019).
32. R. A. Spence, W. M. Kati, K. S. Anderson, K. A. Johnson, Mechanism of inhibition of HIV-1 reverse transcriptase by nonnucleoside inhibitors. *Science* **267**, 988–993 (1995).
33. K. Rittinger, G. Divita, R. S. Goody, Human immunodeficiency virus reverse transcriptase substrate-induced conformational changes and the mechanism of inhibition by nonnucleoside inhibitors. *Proc. Natl. Acad. Sci. U.S.A.* **92**, 8046–8049 (1995).
34. H. Huang, R. Chopra, G. L. Verdine, S. C. Harrison, Structure of a covalently trapped catalytic complex of HIV-1 reverse transcriptase: Implications for drug resistance. *Science* **282**, 1669–1675 (1998).
35. H. T. Xu *et al.*, Effect of mutations at position E138 in HIV-1 reverse transcriptase and their interactions with the M184I mutation on defining patterns of resistance to nonnucleoside reverse transcriptase inhibitors rilpivirine and etravirine. *Antimicrob. Agents Chemother.* **57**, 3100–3109 (2013).
36. R. Kulkarni *et al.*, The HIV-1 reverse transcriptase M184I mutation enhances the E138K-associated resistance to rilpivirine and decreases viral fitness. *J. Acquir. Immune Defic. Syndr.* **59**, 47–54 (2012).
37. H. T. Xu *et al.*, Compensation by the E138K mutation in HIV-1 reverse transcriptase for deficits in viral replication capacity and enzyme processivity associated with the M184I/V mutations. *J. Virol.* **85**, 11300–11308 (2011).
38. M. Feng *et al.*, In vitro resistance selection with doravirine (MK-1439), a novel nonnucleoside reverse transcriptase inhibitor with distinct mutation development pathways. *Antimicrob. Agents Chemother.* **59**, 590–598 (2015).
39. M. Feng *et al.*, Doravirine suppresses common nonnucleoside reverse transcriptase inhibitor-associated mutants at clinically relevant concentrations. *Antimicrob. Agents Chemother.* **60**, 2241–2247 (2016).
40. S. J. Smith *et al.*, Rilpivirine and doravirine have complementary efficacies against NNRTI-resistant HIV-1 mutants. *J. Acquir. Immune Defic. Syndr.* **72**, 485–491 (2016).
41. M. Oliveira *et al.*, M184I/V substitutions and E138K/M184I/V double substitutions in HIV reverse transcriptase do not significantly affect the antiviral activity of EFdA. *J. Antimicrob. Chemother.* **72**, 3008–3011 (2017).
42. X. P. Song, C. Bouillon, E. Lescrinier, P. Herdewijn, Iminodipropionic acid as the leaving group for DNA polymerization by HIV-1 reverse transcriptase. *ChemBioChem* **12**, 1868–1880 (2011).

43. R. F. Schinazi *et al.*, Characterization of human immunodeficiency viruses resistant to oxathiolane-cytosine nucleosides. *Antimicrob. Agents Chemother.* **37**, 875–881 (1993).
44. M. Tisdale, S. D. Kemp, N. R. Parry, B. A. Larder, Rapid in vitro selection of human immunodeficiency virus type 1 resistant to 3′-thiacytidine inhibitors due to a mutation in the YMDD region of reverse transcriptase. *Proc. Natl. Acad. Sci. U.S.A.* **90**, 5653–5656 (1993).
45. M. Hung *et al.*, Elucidating molecular interactions of *L*-nucleotides with HIV-1 reverse transcriptase and mechanism of M184V-caused drug resistance. *Commun. Biol.* **2**, 469 (2019).
46. S. G. Sarafianos *et al.*, Lamivudine (3TC) resistance in HIV-1 reverse transcriptase involves steric hindrance with beta-branched amino acids. *Proc. Natl. Acad. Sci. U.S.A.* **96**, 10027–10032 (1999).
47. S. Liu, E. A. Abbondanzieri, J. W. Rausch, S. F. Le Grice, X. Zhuang, Slide into action: Dynamic shuttling of HIV reverse transcriptase on nucleic acid substrates. *Science* **322**, 1092–1097 (2008).
48. S. E. Martinez, J. D. Bauman, K. Das, E. Arnold, Structure of HIV-1 reverse transcriptase/d4TTP complex: Novel DNA cross-linking site and pH-dependent conformational changes. *Protein Sci.* **28**, 587–597 (2019).
49. V. L. Singer, L. J. Jones, S. T. Yue, R. P. Haugland, Characterization of PicoGreen reagent and development of a fluorescence-based solution assay for double-stranded DNA quantitation. *Anal. Biochem.* **249**, 228–238 (1997).
50. S. Q. Zheng *et al.*, MotionCor2: Anisotropic correction of beam-induced motion for improved cryo-electron microscopy. *Nat. Methods* **14**, 331–332 (2017).
51. J. Zivanov *et al.*, New tools for automated high-resolution cryo-EM structure determination in RELION-3. *eLife* **7**, e42166 (2018).
52. A. Rohou, N. Grigorieff, CTFFIND4: Fast and accurate defocus estimation from electron micrographs. *J. Struct. Biol.* **192**, 216–221 (2015).
53. P. Emsley, K. Cowtan, Coot: Model-building tools for molecular graphics. *Acta Crystallogr. D Biol. Crystallogr.* **60**, 2126–2132 (2004).
54. P. V. Afonine *et al.*, Real-space refinement in PHENIX for cryo-EM and crystallography. *Acta Crystallogr. D Struct. Biol.* **74**, 531–544 (2018).
55. E. F. Pettersen *et al.*, UCSF Chimera–A visualization system for exploratory research and analysis. *J. Comput. Chem.* **25**, 1605–1612 (2004).
56. A. K. Singh *et al.*, Cryo-EM structures of wild-type and E138K/M184I mutant HIV-1 RT/DNA complexed with inhibitors doravirine and rilpivirine. EMDB. https://www.ebi.ac.uk/emdb/search/EMD-14457. Deposited 25 February 2022.
57. A. K. Singh *et al.*, Cryo-EM structure of HIV-1 reverse transcriptase with a DNA aptamer in complex with nevirapine. PDB. https://www.rcsb.org/structure/unreleased/7Z24. Deposited 25 February 2022.
58. A. K. Singh *et al.*, Cryo-EM structures of wild-type and E138K/M184I mutant HIV-1 RT/DNA complexed with inhibitors doravirine and rilpivirine. EMDB. https://www.ebi.ac.uk/emdb/search/EMD-14458. Deposited 26 February 2022.
59. A. K. Singh *et al.*, Cryo-EM structure of NNRTI resistant M184I/E138K mutant HIV-1 reverse transcriptase with a DNA aptamer in complex with nevirapine. PDB. https://www.rcsb.org/structure/unreleased/7Z29. Deposited 26 February 2022.
60. A. K. Singh *et al.*, Cryo-EM structures of wild-type and E138K/M184I mutant HIV-1 RT/DNA complexed with inhibitors doravirine and rilpivirine. EMDB. https://www.ebi.ac.uk/emdb/search/EMD-14462. Deposited 26 February 2022.
61. A. K. Singh *et al.*, Cryo-EM structure of HIV-1 reverse transcriptase with a DNA aptamer in complex with rilpivirine. PDB. https://www.rcsb.org/structure/unreleased/7Z2D. Deposited 26 February 2022.
62. A. K. Singh *et al.*, Cryo-EM structures of wild-type and E138K/M184I mutant HIV-1 RT/DNA complexed with inhibitors doravirine and rilpivirine. EMDB. https://www.ebi.ac.uk/emdb/search/EMD-14463. Deposited 26 February 2022.
63. A. K. Singh *et al.*, Cryo-EM structure of NNRTI resistant M184I/E138K mutant HIV-1 reverse transcriptase with a DNA aptamer in complex with rilpivirine. PDB. https://www.rcsb.org/structure/unreleased/7Z2E. Deposited 26 February 2022.
64. A. K. Singh *et al.*, Cryo-EM structures of wild-type and E138K/M184I mutant HIV-1 RT/DNA complexed with inhibitors doravirine and rilpivirine. EMDB. https://www.ebi.ac.uk/emdb/search/EMD-14465. Deposited 26 February 2022.
65. A. K. Singh *et al.*, Cryo-EM structure of HIV-1 reverse transcriptase with a DNA aptamer in complex with doravirine. PDB. https://www.rcsb.org/structure/unreleased/7Z2G. Deposited 26 February 2022.
66. A. K. Singh *et al.*, Cryo-EM structures of wild-type and E138K/M184I mutant HIV-1 RT/DNA complexed with inhibitors doravirine and rilpivirine. EMDB. https://www.ebi.ac.uk/emdb/search/EMD-14466. Deposited 27 February 2022.
67. A. K. Singh *et al.*, Cryo-EM structure of NNRTI resistant M184I/E138K mutant HIV-1 reverse transcriptase with a DNA aptamer in complex with doravirine. PDB. https://www.rcsb.org/structure/unreleased/7Z2H. Deposited 27 February 2022.